Supplemental Information

Molecular Electronics Sensors on a Scalable CMOS Chip: A Platform for Single-Molecule Measurement of Binding Kinetics & Enzyme Activity

Authors: *Carl W. Fuller[a], Pius S. Padayatti[a], Hadi Abderrahim[a], Lisa Adamiak[a], Nolan Alagar[a], Nagaraj Ananthapadmanabhan[a], Jihye Baek[a], Sarat Chinni[a], Chulmin Choi[a], Kevin J. Delaney[a], Rich Dubielzig[a], Julie Frkanec[a], Chris Garcia[a], Calvin Gardner[a], Daniel Gebhardt[a], Tim Geiser[a], Zachariah Gutierrez[a], Andrew P. Hodges[a], Guangyuan Hou[a], Sonal Jain[a], Teresa Jones[a], Raymond Lobaton[a], Zsolt Majzik[a], Allen Marte[a], Prateek Mohan[a], Paul Mola II[a], Paul Mudondo[a], James Mullinix[a], Thuan Nguyen[a], Frederick Ollinger[a], Sarah Orr[a], Yuxuan Ouyang[a], Paul Pan[a], Namseok Park[a], David Porras[a], Keshav Prabhu[a], Cassandra Reese[a], Travers Ruel[a], Trevor Sauerbrey[a], Jaymie R. Sawyer[a], Prem Sinha[a], Jacky Tu[a], AG Venkatesh[a], Sushmitha VijayKumar[a], Le Zheng[a], Drew A. Hall[a,b], Sungho Jin[c], James M. Tour[d], George M. Church[e], Paul W. Mola[a], Barry Merriman[a]*

Corresponding Author*: George Church (gc@hms.harvard.edu)*
Additional Corresponding Author*: Barry Merriman (barry.merriman@roswellbiotech.com)*

This PDF file includes:

Characteristics of an ideal semiconductor chip biosensor.

The full potential of this vision of moving molecular biosensing "on-chip" can only be realized by using a suitably compatible sensor concept. To this end, there are three fundamental sensor design principles to consider—*manufacturability*, *scalability*, and *universality*:

Manufacturability: It is essential that the required chip be fully manufacturable within existing CMOS foundry fabrication processes, to leverage the mass-manufacturing base and economy of scale. It is also critical that any other sensor-related elements are also mass-manufacturable using existing industrial processes. Otherwise, if novel manufacturing capabilities must be created, it can take decades to achieve economic parity with current standard CMOS chip manufacturing.

Scalability: It is essential to solve the "More-than-Moore" problem, which limits the scalability of chip-based approaches: devices with non-CMOS features often cannot keep up with the pace of scaling of Moore's Law. Thus, an on-chip sensor concept should in no way impede miniaturization of the circuits. The ideal solution is to have the sensor element be "fully scaled" at the onset, i.e., already at the nanometer scale, so no further changes are required as the supporting CMOS measurement circuitry is miniaturized.

Universality: It is essential to have a universal sensor concept, so that one platform can serve the great diversity of biosensing applications and meet the most demanding specifications. The range of biosensing *targets* includes small molecules, antigens, proteins, antibodies, aptamers, DNA, RNA, enzymes and their substrates. Performance specifications ideally extend to the limits of such measurements, including single-molecule, real-time and label-free detection.

CMOS Molecular Electronics sensor chips: pixel and chip architecture, device fabrication, and characterization.

The CMOS sensor array chips used in this study were designed at Roswell Biotechnologies Inc. and fabricated at TSMC, Ltd. in Taiwan, using a 180nm CMOS node foundry. The design and layout were done using design tools from Cadence Design Systems, Inc. These chips present a 16k (16,384) sensor pixel array. Pixels are post-processed at the IMEC foundry (Leuven, Belgium) to have the tips of Ruthenium nano-electrodes exposed on the solution-facing surface of the chip, with such electrodes fabricated using either photolithography or e-beam lithography methods. The 16k electrodes were fabricated to have various nano-gap sizes in different ranges: 10-12 nm, 14-16 nm, 17-20nm and 20-30 nm. Gaps of 14-20 nm were used for present experiments, and other sizes were not analyzed for present experiments. The chips were mounted in custom-built instruments to support chip operations and sensor pixel data collection. The data are collected from the 16k sensor array at a frame rate of 1000Hz, and current measurements have 10 bits of resolution.

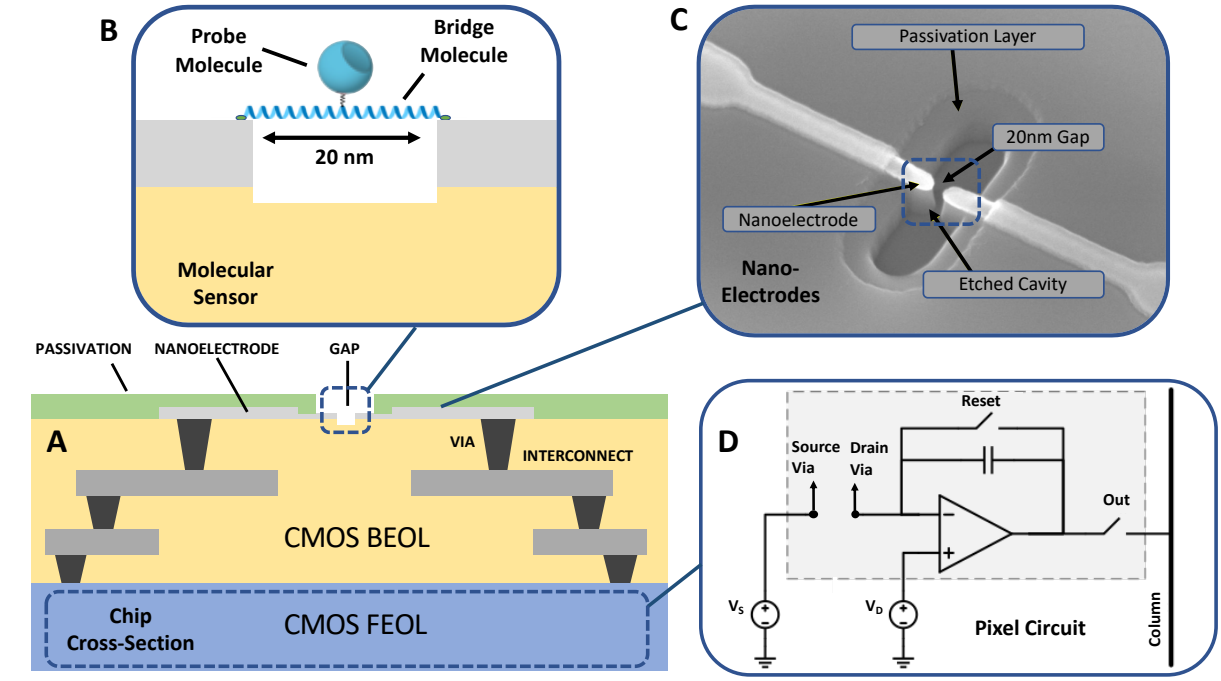
B
Probe Molecule
Bridge Molecule
20 nm
Molecular Sensor
C
Passivation Layer
20nm Gap
Nanoelectrode
Etched Cavity
Nano-Electrodes
PASSIVATION
NANOELECTRODE
GAP
A
VIA
INTERCONNECT
CMOS BEOL
Chip Cross-Section
CMOS FEOL
D
Reset
Source Via
Drain Via
Out
Pixel Circuit
Column

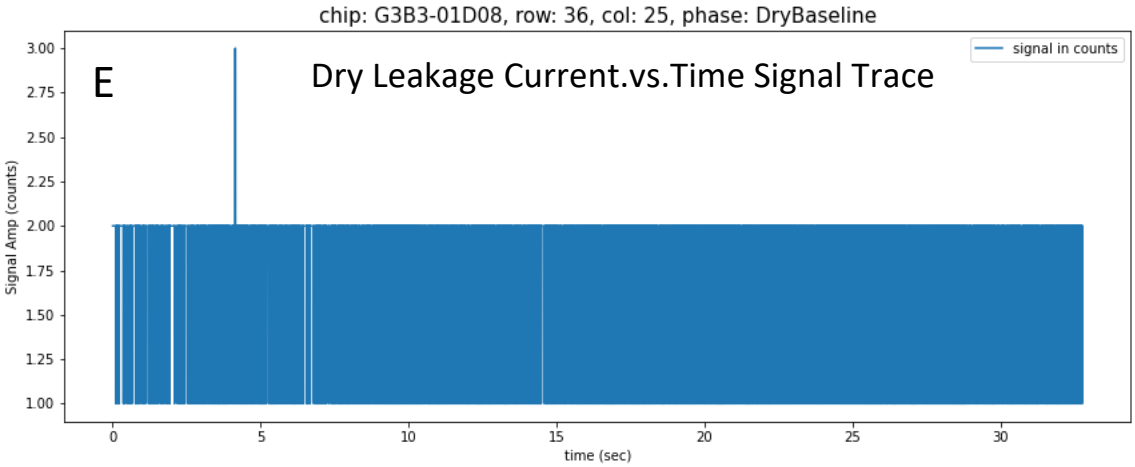
chip: G3B3-01D08, row: 36, col: 25, phase: DryBaseline
E
Dry Leakage Current.vs.Time Signal Trace
signal in counts
Signal Amp (counts)
time (sec)

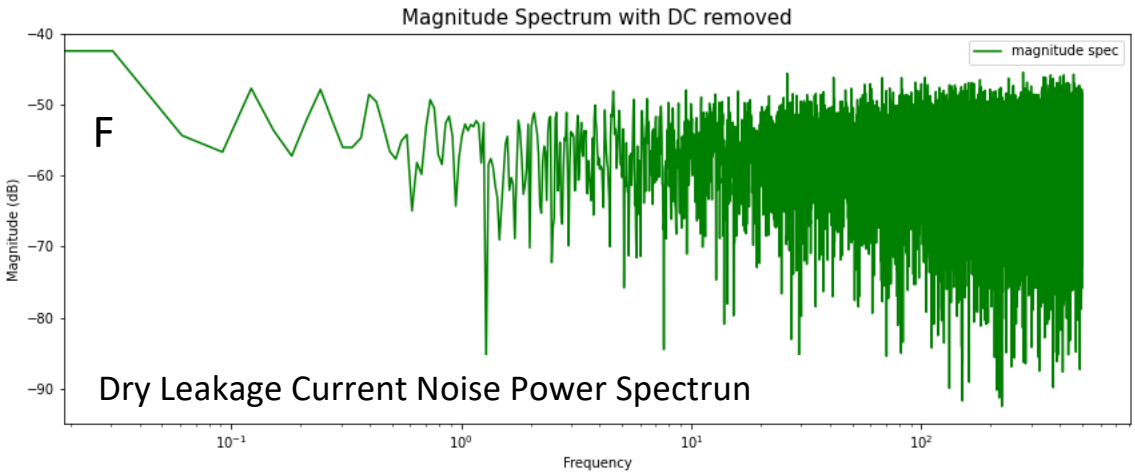
Magnitude Spectrum with DC removed
F
magnitude spec
Magnitude (dB)
Frequency
Dry Leakage Current Noise Power Spectrun

Fig. S1A. CMOS Molecular Electronics Sensor Pixel. The sensor pixel concept is fabricated in CMOS as shown: (A) Cross-Sectional illustration of the CMOS layer stack-up, consisting of the Front-End-Of-Line (FEOL) transistor layers, and the Back-End-Of-Line (BEOL) layers providing metal interconnects (lateral wires) and vias (vertical wires). This shows how nano-electrodes fabricated at an upper planar layer are connected down into the transistor layer using a series of vias and interconnects. (B) Illustration of how the idealized molecular sensor is configured in the exposed nano-electrodes. (C) Electron micrograph of actual chip nanoelectrodes, fabricated by CMOS-foundry compatible photo-lithography processes, to have an approximately 20nm gap open for the molecular wire. (D) The pixel measurement circuit is shown schematically. This is located within the FEOL layers. As indicated, the measurement circuit integrates current flowing through one electrode (referred to as the "drain" side) onto a capacitor, for readout by switching into off-pixel array column circuits. Source and drain side inputs in turn are connected to the nanoelectrode and sensor molecular wire using the vias and interconnects as shown. (E) Representative signal trace from a pixel on a dry chip, showing level of electronic noise and baseline leakage current that would be present prior to beginning a wet experiment of the type reported herein (chip previously cleaned for use, but no molecules in the nano-gap, signal measured in air, at 1V DC applied voltage). Current y-axis is in ADC output counts, each count corresponds to ~0.4pA of current. As shown, the signal fluctuates rapidly (comparable to the 1kHz sampling rate) by 1 to 2 ADC counts (~ 0.4 to 0.8 pA) over the 30 seconds of observation. (F) Correspodng power spectrum computed from the trace (with DC offet removed) show the absence of specific noises. The majority of the trace above frequencies of 1Hz reflects pure thermal noise, as ideally expected.

A

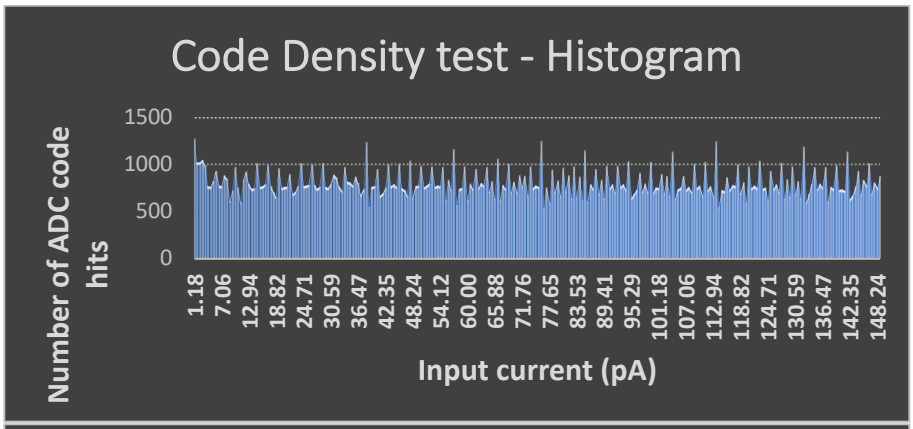

B

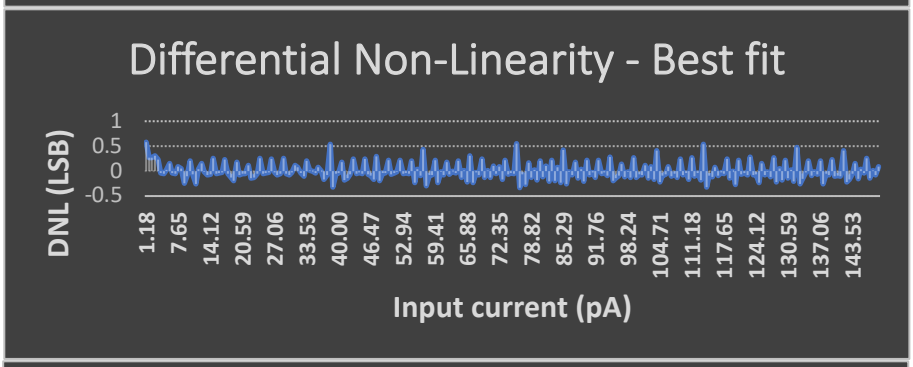

C

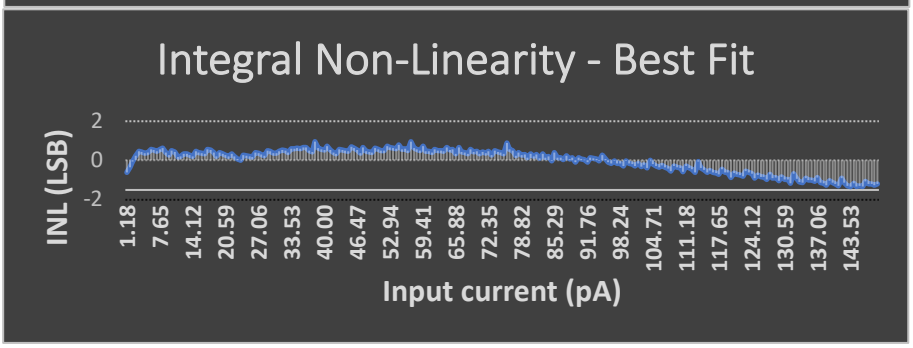

Fig. S1B. Pixel ADC linearity measurements. This shows standard ADC linearity metrics, verifying that the amplifier and ADC are highly linear over the dynamic range of current measurement. Measures are: (A) Uniformity of the ADC code histogram, as the input calibration current is swept linearly from 0 to 150 pA, showing uniform ADC code utilization. (B) Differential Nonlinearity of the ADC, showing less than 1 Least Significat Bit (LSB) of variation. (C) Integral Non-linearity (INL) of the ADC, also generally less than 1 LSB.

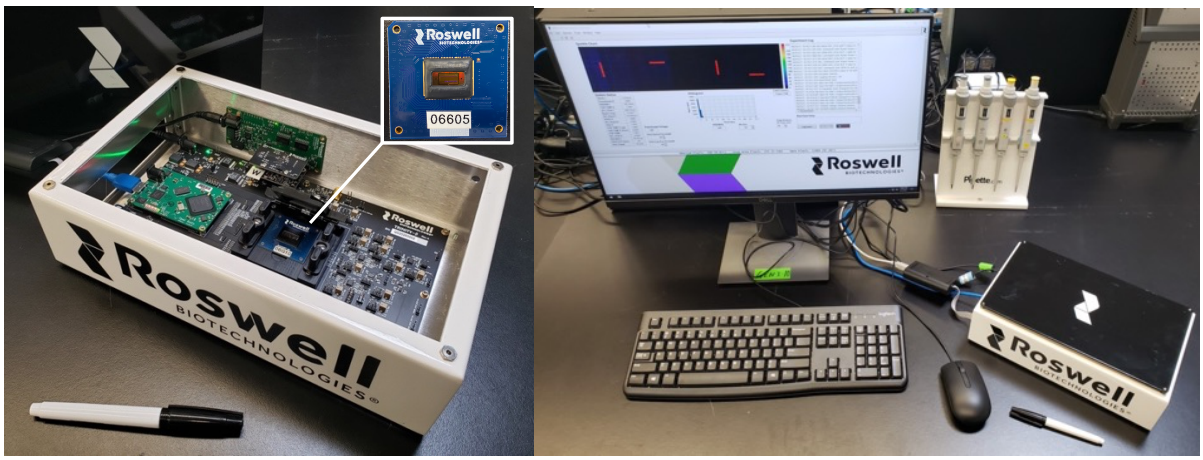

Fig. S1C. Sensor chip deployment instrument used for running experiments in this report. (Left) The 16k sensor CMOS chip is mounted in small form-factor custom-designed instrument. The chip is wirebonded to a PCB interposer board (inset), which mounts in a flow-cell socket in the center of the motherboard. (Right) System control software (seen on screen) runs on an adjacent laptop computer, and data is transferred off-instrument to computer for analysis.

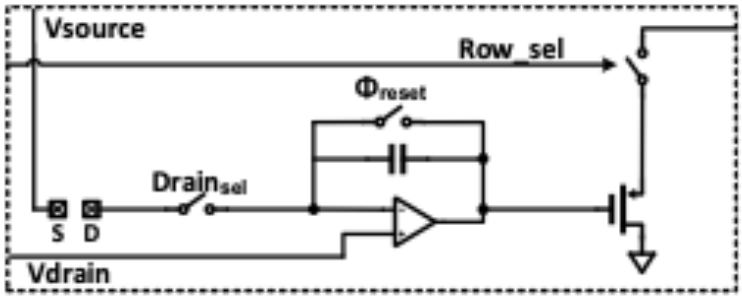

Fig. S1D. CMOS Sensor Pixel Basic Architecture Detail: The major organizational elements of the pixel are as follows, corresponding to the pixel level circuit schematic illustration shown: (1) Each sensor element has a so-called “drain” and “source” electrode, which are spanned by the molecular bridge, and which are distinguished functionally in the circuit in that the actual current measured is the current flowing into the drain: as shown, a switched capacitor transimpedance amplifier is tied to the drain, which integrates the current onto a capacitor while maintaining a constant voltage differential across the source-drain electrode pair. (2) The transimpedance amplifier has a typical gain of 5mV/pA (or 5 Giga-ohm) and dynamic range of 100pA with a root mean square (rms) noise floor of 0.4pA. A high dynamic range option converts the range to 400pA. (3) When the row select switch is on, the stored voltage on the capacitor is transferred to the column ADC for digitization.

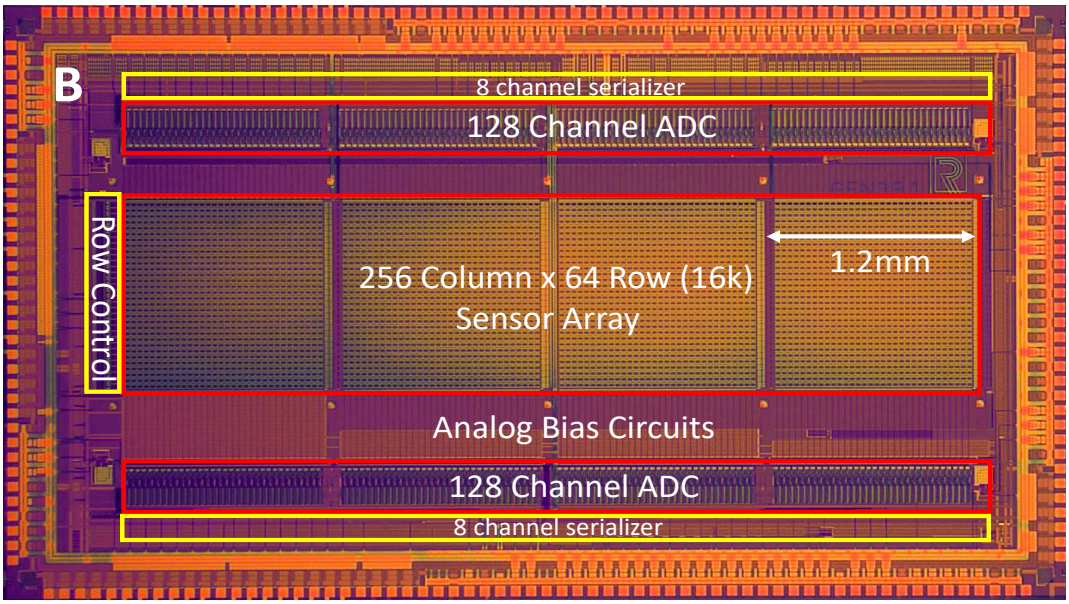

Fig. S1E. Annotated die image for the 16k CMOS sensor array chip. The 16k pixel array is organized as 4 banks of 4k pixels. Readout uses 128 column-pitch-matched ADCs on top and bottom of the device, to read out a full row of 256 pixels, with the Row Selection Control at left. Serializers on top and bottom output the bit data at high speed, supporting the 1000 fps readout.

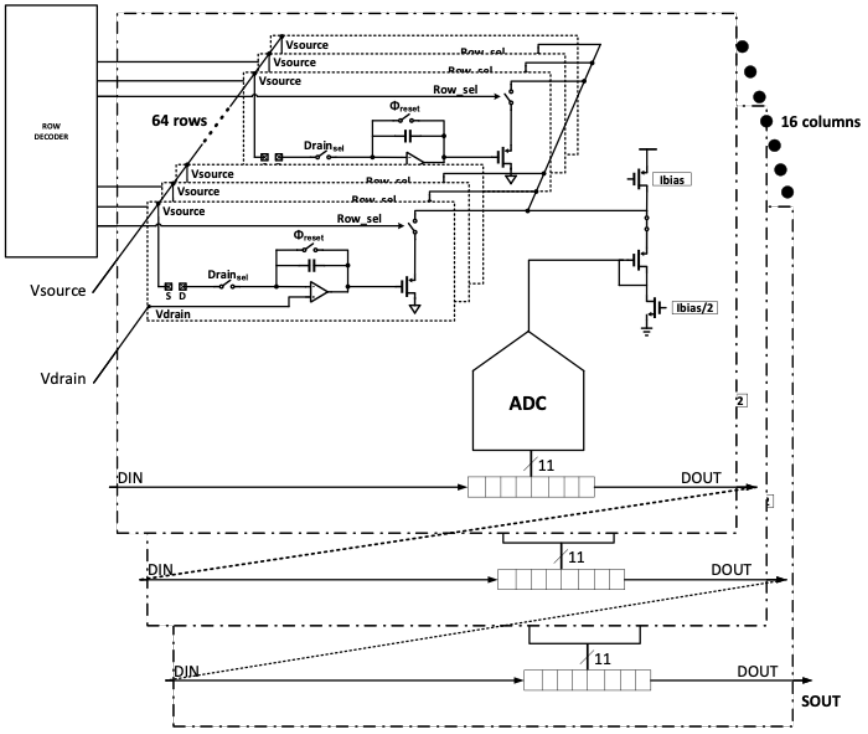

Fig. S1F. CMOS Sensor Array Chip Architecture: The major architectural elements of the sensor array chip of Fig. S1E are as follows, corresponding to the chip-level circuit schematic shown: (1) The chip sensor array organized as 64 rows x 256 columns of pixels (pixel inset shown, and detailed in Fig. S1D) (2) Each column is digitized by an ADC operating at 64K samples/second. (3) 16 ADCs are daisy chained and serialized into a single CMOS 1.8V output at (64Kx16) 1M samples/second implying 11Mbps (bit depth of 11 bits/sample) (4) This in turn can be considered one unit cell of the chip; this unit cell is repeated 16 times to create the 64x256 array. This implies there are 16 parallel output lanes that carry data to the off-chip FPGA, which handles primary off-chip data transfer. (5) There are 256 ADCs in the chip, and they are time interleaved between the 64 rows. (6) The row decoder block is central to the chip and generates the reset and row select control signals for all the rows and facilitates the time interleaved digitization of the 64 rows by 256 different ADCs.

Materials and Methods

Alpha-helix molecular wire bridge preparation.

The peptide is a helix-forming sequence 242 amino acids in length, including an N-terminal

FLAG sequence and metal-binding motifs at each end. In the alpha-helical conformation the

length is ~25nm. A single cysteine residue is present in the middle position as the attachment point for probes using alkyne/azide click chemistry. To attach a DNA to the peptide, it was first modified using a thiol-reactive (1) 3-arylpropiolonitrile (APN)-PEG4- bicyclo [6.1.0] nonyne (BCN) (Conju-Probe, San Diego, CA) yielding a reactive bicyclo nonyne alkyne on the peptide. Typically, 100 µL of peptide solution (3 to 4 mg/mL in PBS) was first mixed with freshly prepared DTT or TCEP (2 mM final) and left at room temperature for an hour. Then the APN-BCN reagent dissolved in DMSO (1 M stock), is added to a final concentration of 0.01 M and mixed thoroughly by pipetting. The reaction is left at 4°C for a minimum of 48 hours. The excess APN-BCN is removed by size-exclusion chromatography. The purified peptide-BCN is stored at -20°C until needed. Further reactions are done using DNA or RNA oligos with azide placed at a specific site to obtain the bridges used in this study. The reaction of BCN with azide was performed in PBS with a molar excess of the oligo-azide to purified peptide-BCN. The final reaction product was further chromatographically purified to more than 95%. The oligos were blocked at the free 3' end with a fluorescent dye (FAM or Cy3 to help detection of peptide on SDS-PAGE). A gel shift on SDS-PAGE confirmed the bridge conjugation to oligos.

Sequences of oligos used in this study as DNA probes:

17mer- TACGTGCAGGTGACAGG/FAM/

45mer- CGATCAGGCCTTCACAGAGGAAGTATCCTCGTTTAGCATACCC/FAM/

DNA oligo binding experiments.

All oligo binding experiments performed in a buffer 50 mM Tris HCl pH 7.5, 4 mM DTT, 10 mM KCl and 10 mM $SrCl_2$ (Buffer A). Primer P-3 binds with its 3' terminus 3 nucleotides away from the bridge; the sequence is 5'-CCTGTCACCTGCAC, complementary to the 17mer.

DNA melting temperature experiments and T_m estimation.

All temperature melt experiments were using the 45mer probe-peptide bridges. The two oligos used in this analysis are 2P-0: CCTCTGTGAAGGCCTGATCG and 2P-5: CCTCTGTGAAGGCCT. The temperature changes were controlled by the software interface that communicates with a Peltier device sitting attached to the chips. The temperature ramps were recorded as ignore and resume phases while every two-degree step were recorded continuously for four minutes of data collection stabilized at the temperature desired. Fraction bound data were fit for ΔH and ΔS using the method of Petersheim & Turner (2).

DNA mismatch binding experiments.

For assessing the binding kinetics for match and mismatch oligos following oligos designed against the 45mer probe bridge.

Exact Match 5'- CCTCTGTGAAGGCCTGATCG, 1 Mismatch 5'- CCTCTCTGAAGGCCTGATCG, 2 Mismatch 5'- CCTCTGTGAACCCCTGATCG, 3 Mismatch 5'- CCAGAGTGAAGGCCTGATCG. Targets (all 20-mers) were added separately, and binding kinetics monitored to tabulate fraction bound and other parameters.

Aptamer-protein binding experiments.

DNA Aptamers were conjugated to the peptide bridge the same click chemistry of azide to BCN described earlier. The SARS-CoV-2 Nucleocapsid protein (N-protein) was target using a 94-nucleotide DNA aptamer /5AzideN//iCy3/TTTTTTGCAATGGTACGGTACTTCCGG ATGCGGAAACTGGCTAATTGGTGAGGCTGGGGCGGTCGTGCAGCAAAAGTGCACGC TACTTTGCTAA (3, 4). The SARS-CoV-2 Spike Protein (S-protein) was targeted using a 57-

mer DNA aptamer /5AzideN//iCy3/TTTTTTCAGCACCGACCTTGTGCTTTGGGAGTGC TGGTCCAAGGGCGTTAATGGACA (5). SARS-CoV-2 Spike Protein (S-protein) (RBD, His Tag) (CatalogNumber:40592-V08B) was purchased from Sino Biological. The protein was analyzed using an SDS-PAGE to confirm the identity of the protein by molecular weight and purity. The control experiments used the Influenza A H1N1 (A/California/07/2009) Nucleoprotein / NP Protein (His Tag) Sino Biological (CatalogNumber:40205-V08B).

DNA polymerase binding experiments.

E. coli DNA polymerase I, Klenow Fragment (3' to 5' exo$^-$) (New England Biolabs, Cat No: M0212M, 75.7 μM) was used for this study. For these experiments, the peptide bridge had the standard 45-mer oligo attached at its 5' end and was annealed to a complementary 35-mer such that its free 3' end was positioned 10 bases from the bridge attachment point, providing a binding site for DNA polymerase. These experiments were run in the absence of nucleoside triphosphates without a thermostat in Mg^{2+}-free buffer with $SrCl_2$.

Nucleotide binding experiments.

As described above, the 45mer bridge was pre-complexed with a primer, and polymerase in Buffer A with a nucleotide added successively at concentrations of 0, 2.5, 5 and 15 μM, and binding events recorded. The nucleotide used here is a modified dT nucleotide with an anionic peptide tag (6).

Effect of salt on oligo binding.

A 17mer bridge is used in these experiments with a binding oligo P-3 5'-CCTGTCACCTGCAC. The binding oligo concentration was 100nM and the potassium chloride concentration was increased over range of 2mM to 2000mM in 10-fold increments. The assay was performed in Buffer A, except for the concentration of KCl which is titrated as described. Debye length calculations use the standard formula valid for aqueous solutions of low ionic strength,

$$\lambda_D = \frac{0.304\ nm}{\sqrt{I\ (M)}}$$

where I is the Molar ionic strength, as in (7).

Binding of Cas12a endonuclease enzyme.

To use the Cas12a enzyme system, a guide RNA was designed to direct activity to the coding region of the SARS CoV-2 S gene. The chosen sequence (rUrA rArUrU rUrCrU rArCrU rC/iAzideN/rU rGrUrA rGrArU rGrArG rUrCrC rArArC rCrArA rCrArG rArArU rCrU) was synthesized and attached to the sensor bridge peptide using click chemistry as described. The Cas12a enzyme was purchased from Integrated DNA Technologies and used as obtained (Cas12a [Cpf1] V3, #1081068). The target DNA strands (50-mer; 5'-AACTTCTAACTTT AGAGTCCAACCAACAGAATCTATTGTTAGATATCCTA and 5'- TAGGATATCT

AACAATAGATTCTGTTGGTTGGACTCTAAAGTTAGAAGTT) were mixed at equimolar concentrations, heated to 95ºC and slowly cooled to 4ºC.

Antibody binding to fluorescein on 3' end of 45-mer probe.

An FAB fragment (Anti_fluorescein_POD Fab fragment Ref No 1146346910 Roche) at various dilutions was used. The fluorescein amidite modification capping the 3' free end of 45-mer bridge is the target of the antibody binding.

DNA Polymerase Activity.

The polymerase used was an engineered fusion protein, with a Phi29 DNA polymerase fused at the N terminus with the SpyCatcher protein (8). This was conjugated to the SpyTag-bridge conjugate post bridging on to the chip, to assemble the final polymerase activity sensor. The DNA template sequence used was 5'-TTTTTTTTTTTTTTTTTTTTTTTT GGGGGGGGGGGGGGG TCAGTCACGTCTA GATGCAGTCAG and the primer sequence was 5'-CTGACT GCATCTAGACGTGACTGA. Nucleotides dCTP and dATP were supplied for the synthesis at a concentration of 200 μM.

COVID-19 mock assay.

The detection target for a COVID-19 nucleic acid assay a segment of the N-gene. The following oligos are used in positive control experiments: The probe oligo conjugated to the bridge is N1Br21 = /5AzideN//iCy3/CCGCATTACGTTTGGTGGACC. A synthetic complementary oligo target used as positive a control is N1-full-24 = 3'-TGGGGCGTAATGCAAACCACCTGG-5'. The CDC assay for SARS-CoV-2 detection kit (2019-nCov CDC EUA Kit, Cat No. 10006770)

is used for generating positive control samples. PCR amplification using the control plasmid and primers from the kit are used for generating the N-gene PCR products. For on-chip assays the PCR DNA product was either digested with Bacteriophage Lambda Exonuclease (to remove the one phosphorylated + strand) or heat denatured and quick-chilled before using on the chips. For assessing the impact of complex background genomic DNA that may be present in real samples, separate runs were also performed wherein Salmon sperm DNA is added at a concentration of 2 μg/ml. Experiments were also performed by spiking in saliva samples from healthy individuals, and with 10% up to 50% saliva by volume going on the chip, so as to mimic possible sample contamination conditions. Sensor readout was not substantially different from what is shown in Fig. 4A with salmon sperm background..

Attachment of bacteriophage Phi29 DNA Polymerase to the peptide bridge.

An exo$^-$ Phi29 DNA polymerase-SpyCatcher fusion was expressed in *E. Coli* and purified using a combination of three chromatographic steps. The peptide bridge was expressed in *E. Coli* and purified using anti-FLAG resin and reacted with APN-BCN to produce the bridge-BCN conjugate as described above. The N-terminus of the spy Tag peptide was chemically modified with azide for click reaction with BCN (1). To form the final polymerase-bridge complex a 50% excess of the Phi29-Spycatcher (1 μM) was mixed with 0.75 μM bridge-SpyTag and incubated on ice followed by purification by SEC-HPLC. Alternatively, polymerase was attached to bridge-spyTag molecules already attached to the chip.

Analysis of single-molecule binding data using Hidden Markov Models (HMM).

Figs. S2—S4 show a detailed HMM analysis of the segment of data seen in Fig. 2. In this case, the unbound state is identified as a low-current range (~30 pA) and the bound state is identified

as the high current range (50 pA—70 pA). The key fundamental parameters that can be extracted from the HMM segmented signal trace are the individual waiting times between binding events, τ_0, and the individual dwell times spent bound, τ_1 (Fig. S2). As shown in the empirical distributions (Fig. S4) the shorter duration events are more numerous, and their frequency decreases exponentially. The duration of such events can be modeled as random variables, with an exponential probability density distribution, $y = \left(\frac{1}{\bar{\tau}}\right) e^{-}\left(\frac{t}{\bar{\tau}}\right)$, where t is an event duration time, $\bar{\tau}$ is the mean of all the state durations measured. The apparent rate constant for such a stochastic process is $k = \left(\frac{1}{\bar{\tau}}\right)$. The key kinetic rate parameters are the off rate, k_{off}, which is computed from the totality of dwell times, $k_{off} = \left(\frac{1}{\bar{\tau}_1}\right)$, and the on rate, k_{on}, computed from the waiting times, $k_{on} = \left(\frac{1}{\bar{\tau}_0}\right)$. In addition, the total fraction of time spent bound (denoted "Fraction Bound" in figures), is a summary statistic that is readily related to the concentration of the target in solution. By formula, the fraction of time that the probe is bound to the target molecule is given by the sum of all the τ_1 periods divided by the total of both the τ_1 and τ_0 periods: $f_b = \sum \tau_1 / (\sum \tau_1 + \sum \tau_0)$. This can also be conveniently related to the binding affinity of the interaction, K_d, which at the single-molecule level is defined here as the target concentration at which the single probe molecule spends equal time bound and unbound. In accordance with Michaelis-Menten reaction kinetics, the fraction of time bound is expected to scale with molar concentration, $[c]$, like $f_b = F\,(\frac{[c]}{K_d})/(1 + (\frac{[c]}{K_d}))$, where K_d is the empirical binding affinity, which has units of concentration, and F is an empirical dimensionless constant, which is the maximum of the fraction of time bound. Ideally, F=1, but in practice, various forms of steric hinderance could result in the probe not being capable of being bound at all times.

Analysis of single-molecule binding data. Hidden Markov Models (HHM) were constructed in the Pyhton Package HMLearn (https://pypi.org/project/hmmlearn/). Major configuration choices were Gaussian emissions,

Maximum a posteriori estimation of the parameters, and 2-state models. Waiting times, τ_0, and bound times, τ_1, are extracted from signal traces using HMM analysis (see SI Appendix for details). Kinetic rate parameters are computed as: off rate, $k_{off} = \left(\frac{1}{\bar{\tau}_1}\right)$ (here "bar" denotes the mean), on rate, $k_{on} = \left(\frac{1}{\bar{\tau}_0}\right)$ (which is concentration dependent). The fraction of time bound is then given by $f_b = \sum \tau_1 / (\sum \tau_1 + \sum \tau_0) = k_{on} / (k_{on} + k_{off})$. The fraction of time bound is modelled as obeying a classical Michaelis-Menten kinetic formula, depending on target concentration, $[c]$, as $f_b = F\,(\frac{[c]}{K_d}) / (1 + (\frac{[c]}{K_d}))$, where K_d is the empirical binding affinity, which has units of concentration, and F is an empirical constant. Thus, K_d is defined at the single-molecule level of interest here as the target concentration at which the single probe molecule spends equal time bound and unbound.

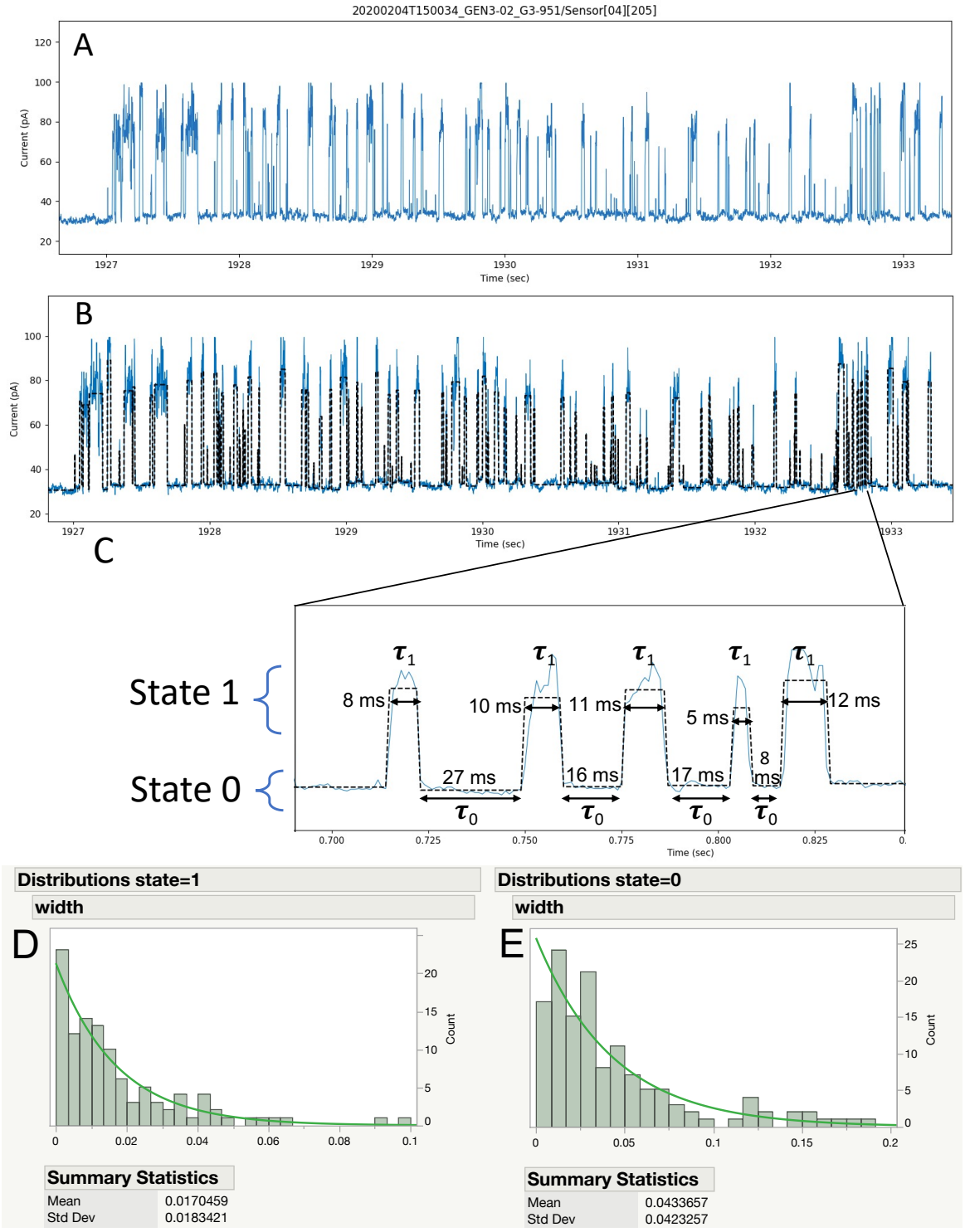

Fig. S2. DNA Binding Signal Trace analysis using a Hidden Markov Model (HMM). Example showing how an HMM can be fit to a current-time trace to quantify information about single-molecule interaction kinetics. (A) Raw data trace from the DNA binding probe sensor of Fig. 2 (1kHz raw sampling rate). (B) The 2-state HMM model fit to the data is shown in (black dashed line) and enlarged in (C) to show the $\boldsymbol{\tau}_0$ (waiting time) and $\boldsymbol{\tau}_1$ (dwell time) parameters for each

binding event. Histograms of the observed τ_0 and τ_1 times are shown in (D) and (E), affirming that both waiting and dwell fit well to an exponential distribution (darker green line), as expected for a first-order stochastic process obeying Boltzmann kinetics (also see Fig. S4).

Table S1. HMM statistics derived from **Fig. S2**

state	count	Mean current	time_in_state (s)	fraction_in_state	mean_time_in_state (s)
0	2950	27.70	299.335	0.904338	0.101469
1	2949	33.35	31.664	0.095662	0.010737

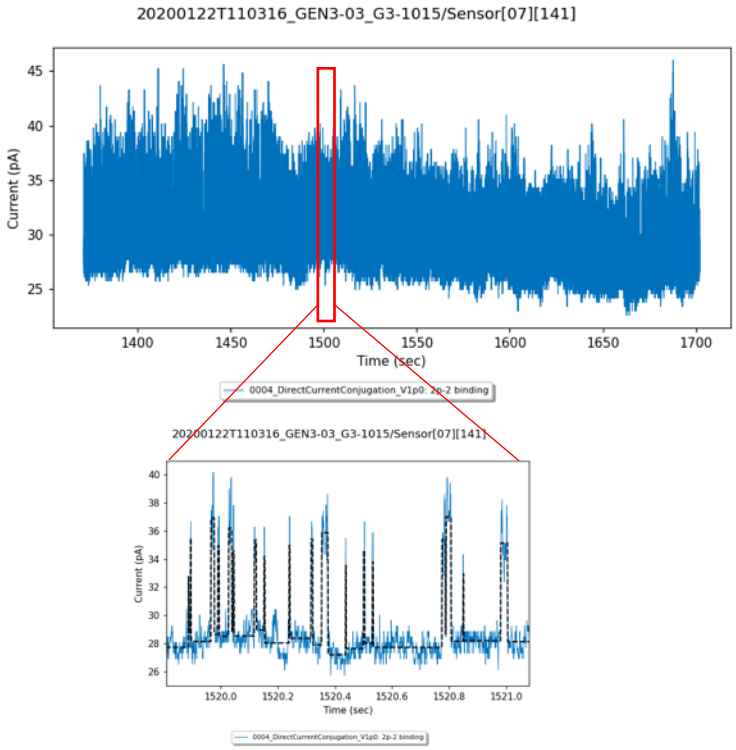

Fig. S3. DNA Binding Signal Trace analysis using a Hidden Markov Model (HMM). In this example, the analysis was of an entire phase (450 seconds) of the DNA probe binding its target at one concentration. Here, the bridge had a 45mer attached at its 5' end (5'-CGATCAGGCCTTCACAGAGGAAGTATCCTGTCGTTTAGCATACCC). The target oligo binding was an 18mer (5'-TCTGTGAAGGCCTGATCG) at 10 nM concentration. Running the HMM on the entire trace extracts 2049 binding events. The resulting summary statistics include (see Table S1) this count of states, an estimate the fraction of time bound, 0.0957, the average waiting time of 0.101 seconds and the average dwell time of 0.0107 s. These in turn allow estimation of the kinetic rates, $k_{off} = 1/0.0107 = 93$ sec $^{-1}$ and $k_{on} = 1/ (0.101 \times 10^{-7}) = 9.9 \times 10^7$ M^{-1} sec^{-1} (this makes use of the fact that in an ideal exponential distribution the mean of all the τ_n states is equal to the reciprocal of the decay constant). More sophisticated analyses may be needed if the distribution diverges far from the ideal case. This experiment was carried out at

room temperature, but on-chip temperature for this experiment was not controlled and may be locally higher than ambient. Based on the oligo melting point and observed fraction-of-time bound, it would be consistent with bulk behavior at ~ 50 degrees C.

Table S2. Various Control Targets in the Covid-19 mock assay (supporting legend in **Fig. 4**).

	Name	Control Type	Length	Match Length
a.	Synthetic 24mer Complement	POSITIVE	24	21
b.	Synthetic mock PCR product Reverse Strand	POSITIVE	72	21
c.	Synthetic mock PCR product Forward Strand	NEGATIVE	72	-
d.	Lambda exo-treated PCR product Forward	NEGATIVE	72	-
e.	Lambda exo-treated PCR product Reverse	POSITIVE	72	21
f.	31mer (Unrelated Sequence)	NEGATIVE	31	-
g.	dsDNA PCR product (heat denatured & chilled)	POSITIVE	72	21

Visualizations of Molecular Electronics sensors.

The sensors as shown in Fig. 2, Fig. S7, and throughout the paper, were visualized as follows: All solid and ribbon models and atoms/molecules were visualized using the ChimeraX program (https://www.rbvi.ucsf.edu/chimerax/), version 1.2 (2021-05-24).

The bridge molecule 25nm alpha-helix is the exact amino acid sequence of the molecular wire peptide folded and visualized within ChimeraX. All other molecules used are scaled to be in proportion relative to the 25nm length of the bridge. The small-molecule conjugation between the bridge and probe is indicated schematically by a short, black zig-zag line, as is the conjugation between the fluorescein and tether oligo in Fig. 3G The respective other molecules shown are PDB structures as follows: DNA oligo probe/target (3A) custom sequences input and visualized as DNA helices; Klenow polymerase from 1KFD (4A,C); SARS-CoV-2-Spike Protein from 6VSB, and the S aptamer is the exact Aptamer DNA sequence, folded into a 3D secondary structure using RNAComposer (http://rnacomposer.cs.put.poznan.pl), with structure

visualized in ChimeraX (4E); Antibody from 1IGT (4G); Cas12a from 5B43 (3I); Phi29 Polymerase from 2PYL, combined with SpyTag-SpyCatcher conjugation complex 4MLS (5A).

Pulse analysis of Phi29 DNA Polymerase enzyme activity.

Median and Gaussian filters were applied to the primary trace (Fig. S7A) to filter out narrow and low amplitude pulses classified as noise, based on the characteristics of pulses seen in negative control experiments. A two state HMM with a Gaussian Emission model was used to segment out pulses for analysis. A total of 40 pulses resulted, which matches the length of the template. 7 features metrics were computed for each of the 40 pulses (Fig 5C) (Table S3, SI Appendix). The features are minimum within the pulse, maximum within the pulse, mean across the pulse, standard deviation of across the pulse, time width of the pulse, total number of extrema (local maxima and local minima) within the pulse, and waiting time to the start of the next pulse. These 7 features of each pulse were the inputs to a Principal Component Analysis (PCA). The first two principal components (PC1, PC2) (Fig. S7B) were used to perform K-means clustering of the 40 pulses, with two clusters specified. A total of 16/40 of the pulses fell into cluster 1, and 26/40 pulses fell into cluster 2. When relating these clusters to each pulse position on the trace (Fig 5A), the 16 from cluster 1 came from the first region of expected C incorporations (red), and the 26 from cluster 2 came from the second region of expected A incorporations (green), thus 38 out of 40 (95%) pulses are consistent with putative sequence structure of the trace. The majority of the cluster separation is due to PC1, and the partial contribution of each feature (PCA feature weight) for PC1 is shown in Fig 5C. PCA and K-means clustering analysis done in the JMP software suite (SAS Institute).

Table S3. Pulse Metrics and Cluster Statistics for the Phi29 DNA Polymerase Sensor Pulse Analysis shown in Fig. S6A,B,C and described in Methods.

Cluster Means							
Cluster	min (pA)	max (pA)	mean (pA)	stdev	width (s)	extrema	Waiting time (s)
1	2.945	9.049	5.996	1.898	0.317	3	0.199
2	2.95	4.85	3.975	0.632	0.096	1.083	0.592

Cluster Standard Deviations							
Cluster	min (pA)	max (pA)	mean (pA)	stdev	width (s)	extrema	Waiting time (s)
1	0.03	1.561	0.995	0.522	0.206	2.646	0.208
2	0.007	1.397	0.726	0.473	0.037	0.4	0.591

The features metrics are computed for each of 40 total current pulses segmented from the current-vs-time trace by HMM analysis. The definitions of these features are: min = minimum current within the pulse, max = maximum current within the pulse, mean = mean of the pulse current, stdev = standard deviation of current within the pulse, width = time width of the pulse, extrema = total number of extrema (local maixam and local minima) within the pulse, and waiting time = time interval to the start of the next pulse. These 7 features of each pulse were the inputs to a Principal Component Analysis (PCA), for which the top two components (PC1, PC2) are shown in Fig. S6B. The table below shows the means and deviations of metrics for the two major pulse clusters shown in Fig. S6. The values provided

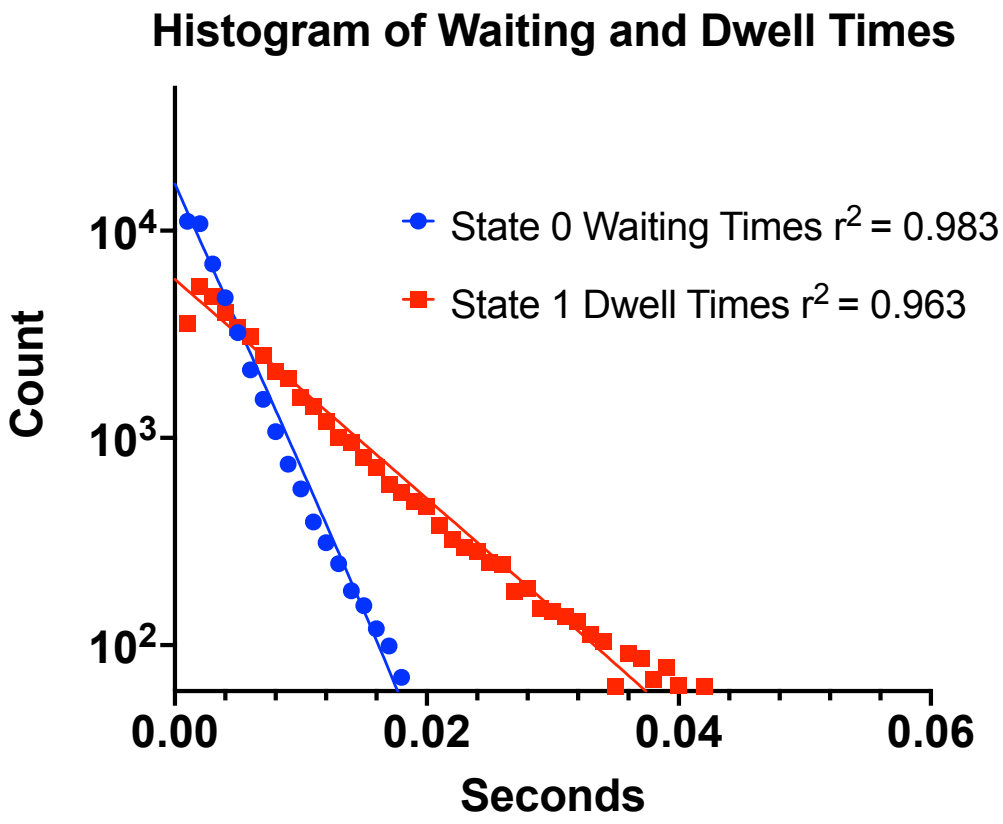

Fig. S4. Exponential Distribution of Binding Parameters for DNA Binding Probe. Data is from the Binding of the 14-mer DNA target to the 17-mer DNA attached to the sensor bridge, as in Fig. 2A. The dwell and waiting times for a total of 44,500 binding events like those shown in Fig. S2 were plotted as distributions to assess fit to an exponential distribution. Both the distributions conform closely to the expected exponential as shown on this semi-log plot, spanning nearly 3 decades, indicating that the binding process in consistent with a single molecule binding reaction with a constant reaction rate, and that the sensor is not substantially distorting the measurements. The temperature of the chip in this experiment was not controlled or recorded but is effectively over 50° C based on the dwell times. From these fits, the mean dwell time is 8.1ms, and the kinetic on/off rates are k_{on} = 3.1 X10^9 $M^{-1}s^{-1}$ and k_{off} = 122 ± 5 sec^{-1}. While the final few data points suggest an additional exponential may be observed, its magnitude is small enough that it does not affect the statistics of the curve fit.

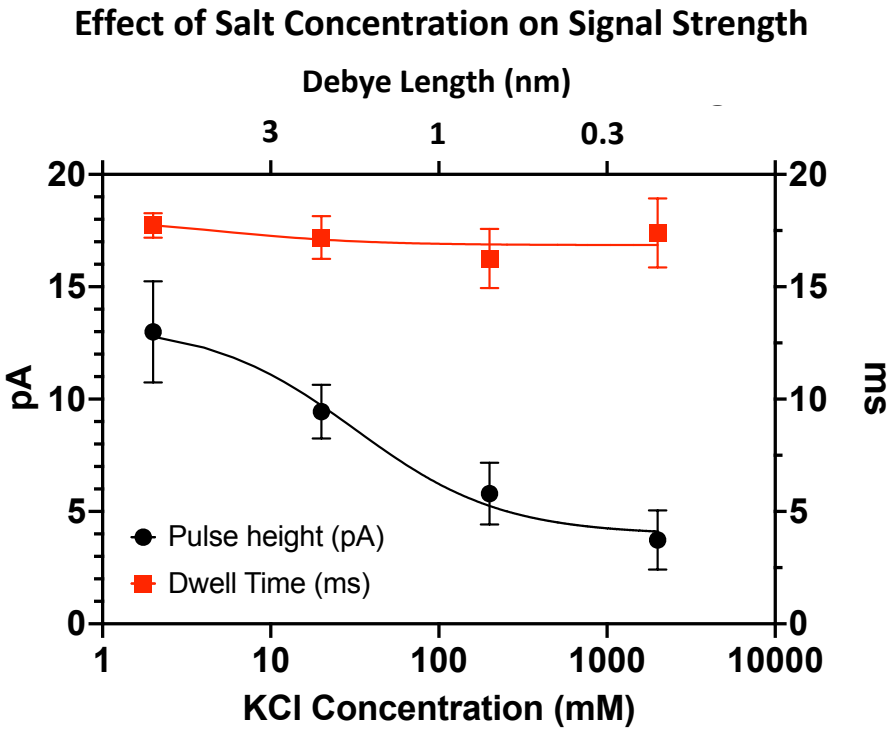

Fig. S5. DNA Binding Probe Response to Titration of Salt Levels. The DNA binding probe and target are the same as in Fig. S2, the 17-mer probe and 14-mer target, with target concentration of 20 nM. The salt concentration of KCl is here titrated from 2 mM to 2000 mM. From resulting traces, kinetic parameters were estimated dwell time (defined as pulse width) and pulse height (a measure of signal strength, defined as the difference between state 0 and state 1 mean currents). As shown, dwell times did not vary significantly with salt, while signal strength in terms of pulse height dropped by approximately 70% in going from 2 mM and 2000 mM, which corresponds to dropping the solution Debye length (electric field decay length) from nearly 10 nm at low salt, down to below 0.3 nm at high salt (solution Debye Length is shown on the upper axes). Results suggest that a substantial component of the signal is due to a field effect arising from charges more than 0.3 nm from the bridge, which is screened out as the Debye length decreases.

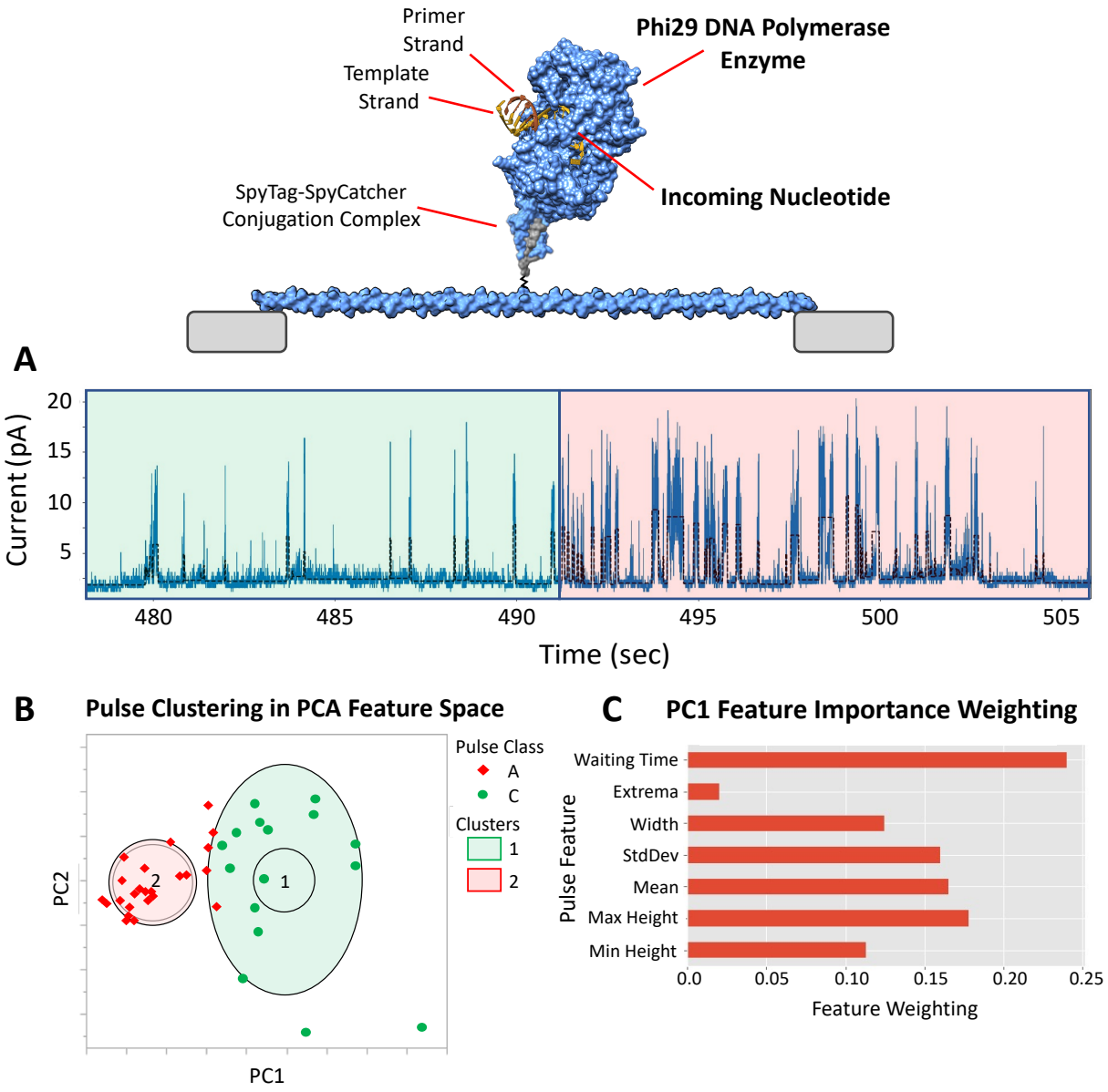

Fig. S6. DNA Polymerase Activity Sensor. (A) A phi29 DNA polymerase is conjugated to the sensor bridge using the SpyTag-SpyCatcher conjugation scheme. A 25-second-long signal trace shows an isolated burst of sensor activity that occurs after adding a primed 40-mer poly G-poly T template and corresponding dCTP and dATP nucleotides to the sensor chip. The blue curve is measured signal data, and the dashed black line indicates an HMM state classification. A series of 40 discrete major pulses are detected, representing putative nucleotide incorporation events (see Methods). The signal trace has wide-spaced, narrower pulses in its left portion, and closely spaced, broader pulses in the right portion, suggesting putative C incorporation (shaded green) vs A incorporation (shaded red) segments corresponging to the template sequence (below). In contrast, in control phases, with either no template DNA or template DNA but no matching nucleotides, only very narrow and small pulses (peak height ~5 pA) are observed. (B) shows the results of a detailed analysis of the pulse features, further supporting the hypothesis that the C and A incorporation pulses are statistically distinguishable (see Methods). For this, an HMM was used to segment out the pulses, and each pulse was annotated with seven extracted features. A Principal Component Analysis (PCA) was performed on these 7 feature metrics, and the pulses are

visualized by plotting projected into the first two principal components space. As shown by a k-means Cluster Analysis, there are two well separated clusters, and the respective red and green color-coded pulses (Pulse Class) from the color-coded segments of trace (A) fall largely into these two clusters, at a 95% concordance level. (C) The weightings of the 7 primary feature metrics onto the first component PC1 are shown. The time between pulses is the major factor, while pulse width and pulse height-related features are also important factors. The quantitative HMM results also suggest C pulses occur at a slower rate (0.68 sec/base) than A pulses (0.29 sec/base), while the C pulses are shorter duration events, at a pulse width of 0.12 seconds, versus A pulses at a width of 0.22 seconds. (See Table S3, SI Appendix). The DNA template was 5'-TTTTTTTTTTTTTTTTTTTTTTTTGGGGGGGGGGGGGGGG TCAGTCACGTCTAGATGCAGTCAG-3' with primer 5'-CTGACT GCATCTAGACGTGACTGA-3', thus the polymerase is expected to incorporate 15 C's followed by 25 A's.

Ribbon Models of Molecular Electronics Sensors and Signal Traces.

Shown below are ribbon models illustrating the sensors used in these studies. These provide more visual detail for complex probe molecules. In addition, exemplar raw signal traces are shown for various of these probes.

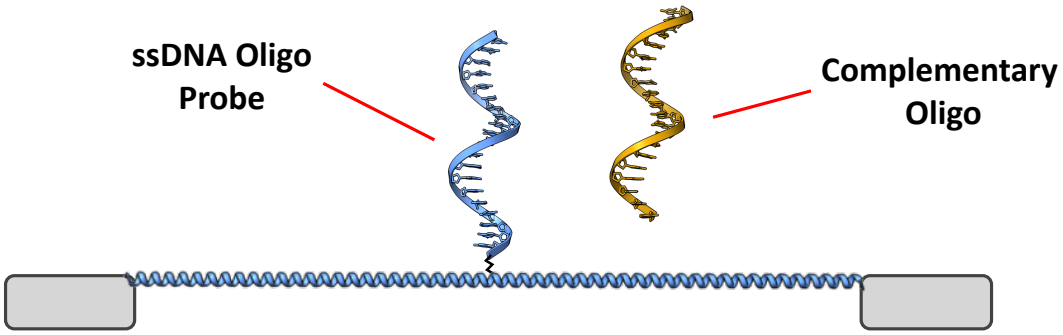

Fig. S7A. DNA Hybridization sensor. A ssDNA Oligo probe is conjugated to the attachment site of the 25nm alpha-helical peptide.

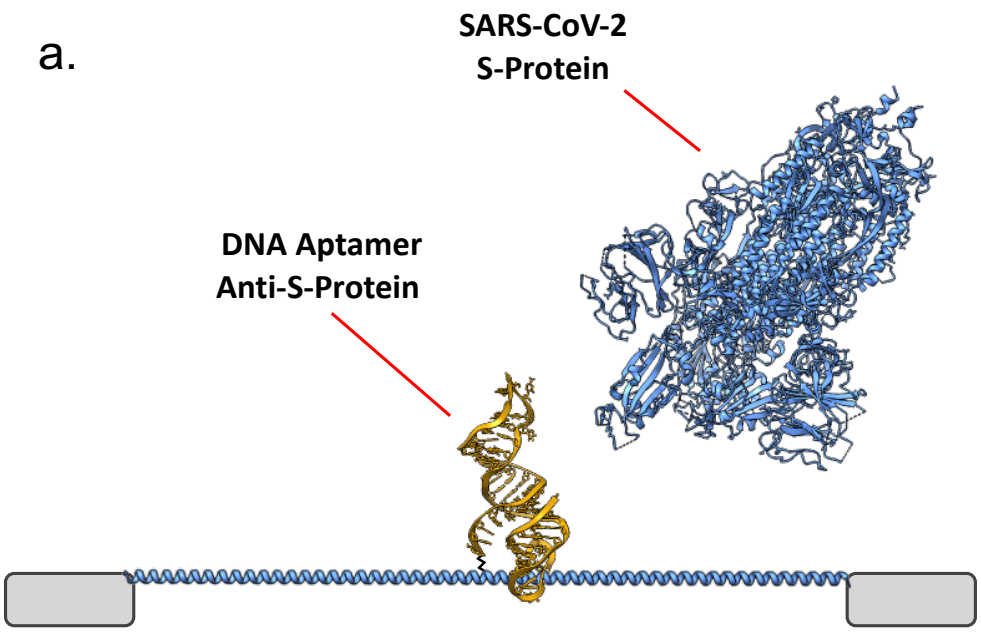

b. Covid Nucleocapsid Protein binding Aptamer Fig. 3F

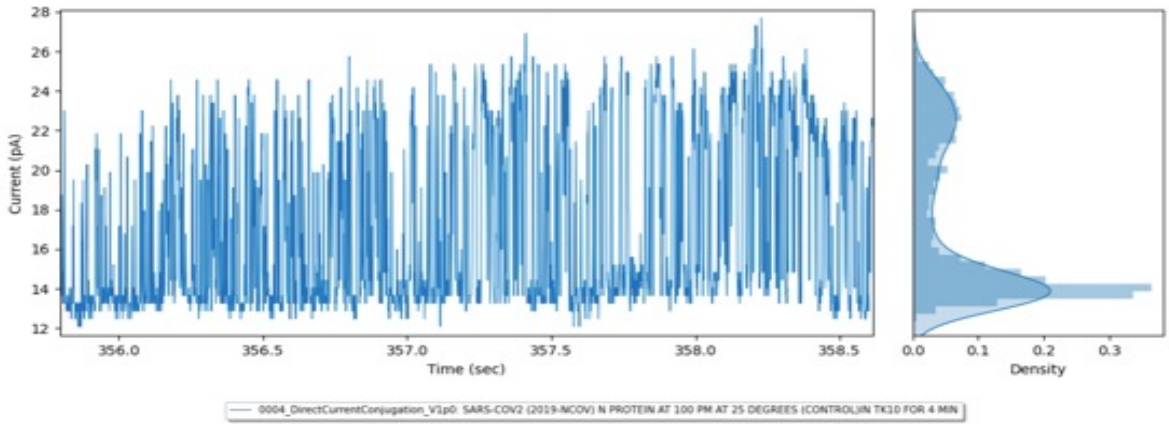

Fig. S7B. a. DNA Aptamer Probe. A ssDNA Aptamer probe is conjugated to the attachment site of the 25nm alpha-helical peptide. Shown is the Aptamer and Target for the SARS-CoV-2 S-Protein. **b.** Raw trace for binding a protein to an aptamer attached to the peptide bridge.

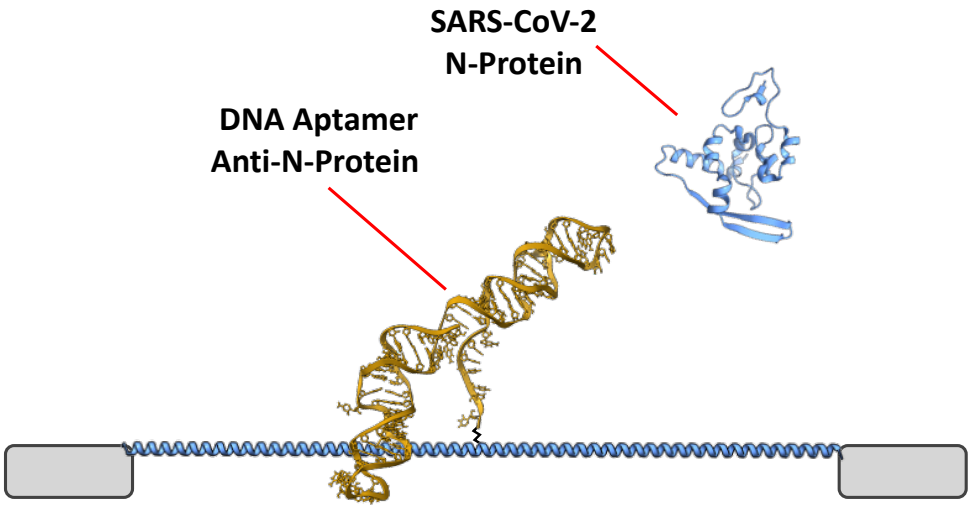

Fig. S7B-2. DNA Aptamer Probe. A ssDNA Aptamer probe is conjugated to the attachment site of the 25nm alpha-helical peptide. Shown is the 94-mer Aptamer and Target for the SARS-CoV-2 N-Protein (N protein dimerization domain shown, PDB 6YUN).

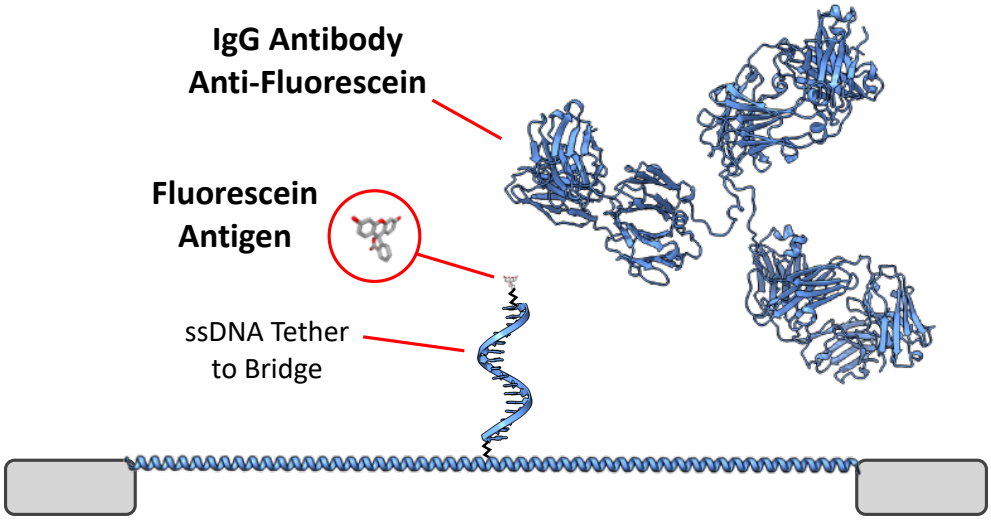

Fig. S7C. Antigen-Antibody Probe. The antigen, here a fluorescein molecule, is tethered to attachment site of the 25nm alpha-helical peptide, using a DNA oligo tether. Shown for perspective is a model Antibody target.

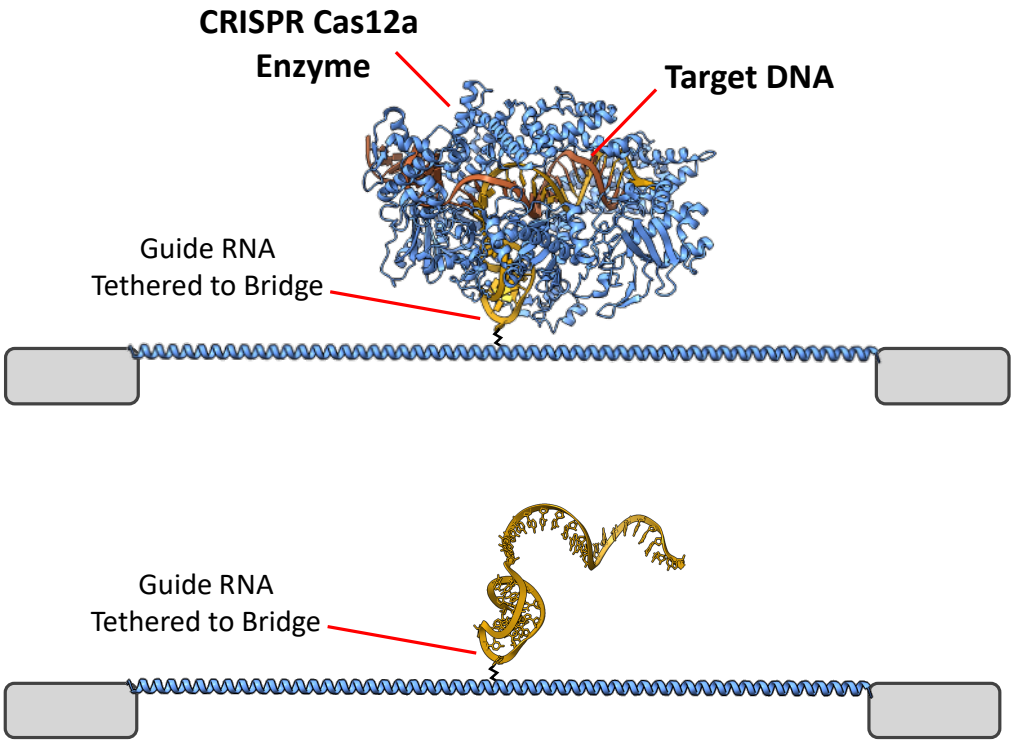

Fig. S7D. (Upper) CRISPR Cas12a Probe for dsDNA target. A guide RNA for a Cas12a enzyme is tethered to the attachment site of the 25nm alpha-helical peptide (Lower), at a site on the RNA that is the most exposed base of the pseudo-knot loop. The Cas12a enzyme is then in turn tethered to the bridge through its docking to the guide RNA. Shown is the resulting cas12a-guide RNA complex interacting with its specific target dsDNA.

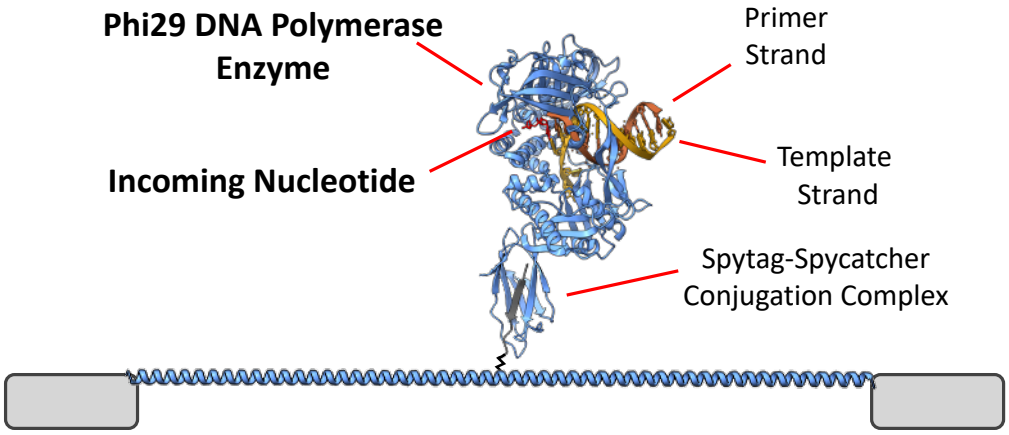

Fig. S7E. DNA Polymerase probe for detecting nucleotide incorporation activity. A Phi29 DNA polymerase is conjugated to the attachment site of the 25nm alpha-helical peptide, using a

SpyTag SpyCatcher conjugation scheme. The spy tag peptide is conjugated to the attachment site on the bridge, and the SpyCatcher motif is fused to the N-terminus of the Phi29 polymerase. Shown is the resulting complex further bound to a primed template DNA and interacting with an incoming nucleotide.

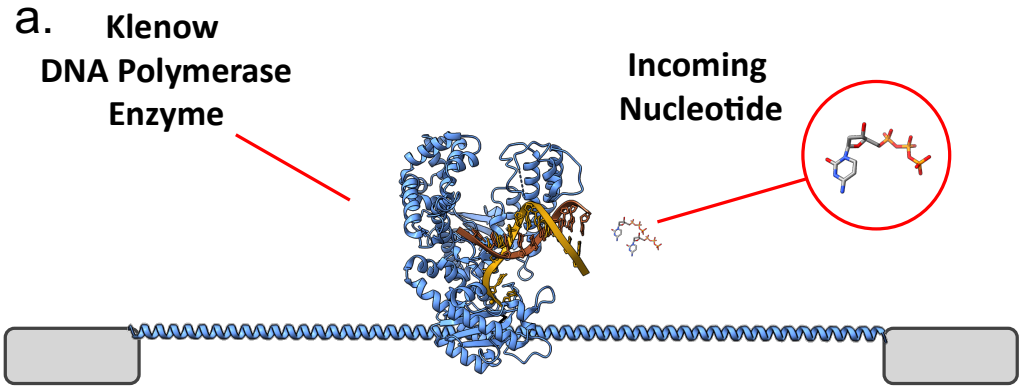

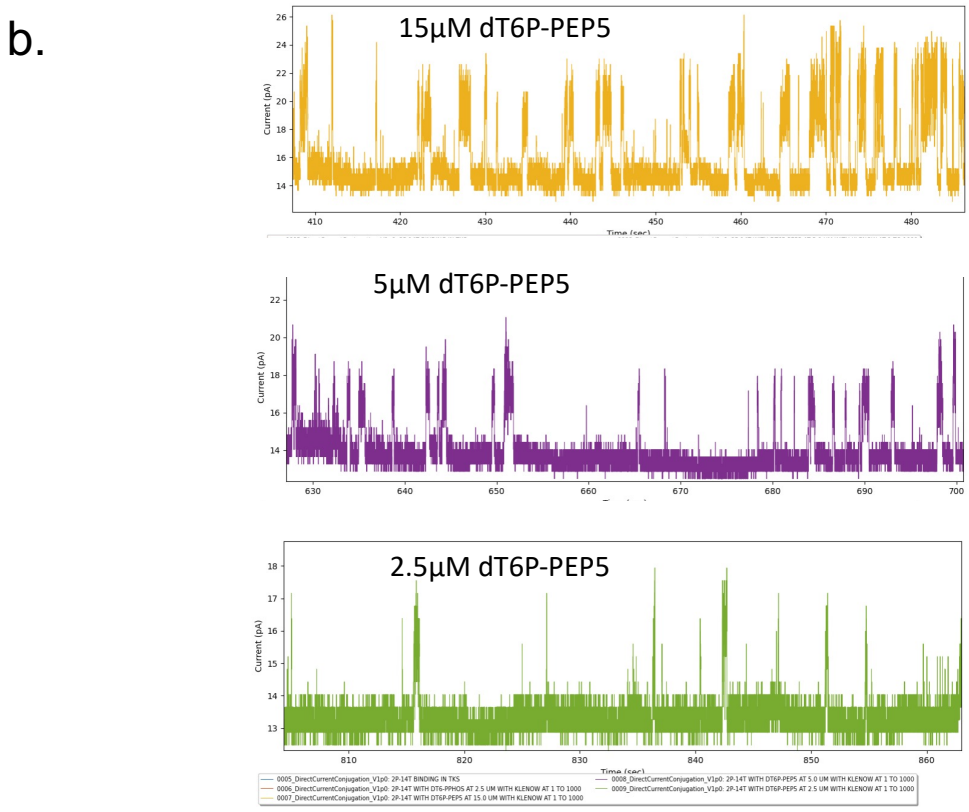

Binding of dT6P-PEP5

Fig. S7F. Small Molecule Binding Probe: Nucleotide Binding in the active pocket of a Klenow DNA Polymerase: **a.** ssDNA template oligo (gold) is conjugated to the attachment site of the 25nm alpha-helical peptide, and a primer oligo is hybridized to this (brown). A Klenow polymerase is recruited to the primer site. Using a non-catalytic buffer (Sr++ replacing Mg++),

this complex interacts with an incoming matched nucleotide (dCTP shown), and in the non-catalytic state, this small molecule binding transiently in the pocket. Thus, this probe complex acts to detect the small molecule binding on a target dNTP. **b**. Raw Data for 3 different concentrations of nucleotide binding (1 min. each) are shown as well (y-axis is current in pA, x-axis is time in seconds).

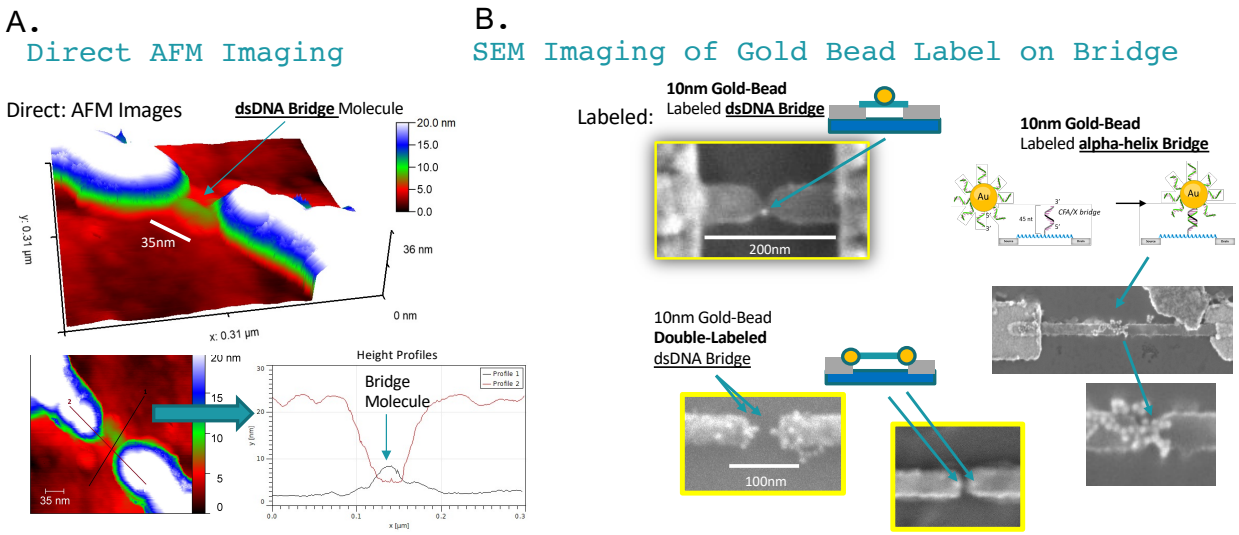

Fig. S7G. Direct imaging of molecular bridges. It would be ideal to directly observe the physical bridge molecules in the nano-electrdoes, but such observations of the single bridge molecules deployed here are beyond the resolution limits of standard fluorescent microscopy, and not readily compatible with common forms of super-resolution fluorescent microscopy (due to presence of metal nano-electrodes). Instead, Atomic Form Microscope (AFM) and Scanning Electron Microscopy (SEM) imaging methods can be used to directly exhibit the location of bridge molecules in the nanoelectrode gap. AFM can directly image molecules without labels, however it is challenging to observe thin molecules (dsDNA is 2nm wide, a peptide alpha-helix is 1.5nm wide), especially when these are short, such as the preferred 25nm bridge length, and it is further challenging to get the AFM tip into the preferred ~20nm nano-electrode gap. For these reasons, the AFM imaging shown was done using a slightly longer dsDNA bridge, in a larger gap. SEM has sub-nm resolution over a broad and general field of view, but single organic molecules do not have sufficient contrast to observe directly, so high-contrast gold-nanoparticle labels are added, to indicate the location of the bridge molecule. This can be a single bead label bound to the conjugation site at the center of the bridge, or two bead labels, one conjugated at each end of the bridge (dumbbell configuration), which also advantageously shows the molecular location more completely. Examples of such imaging results are shown here: (A.) AFM imaging of a 35nm dsDNA bridge between electrodes on chip. Insets show height profiles, and the anticipated ~2nm width of dsDNA. (B.) SEM images of 15nm (upper left) and 25nm (lower left) dsDNA bridges and 25 nm alpha-helical peptide bridges such as are used in the sensors studied herein (right). Gold nanoparticles are used as indicated to label examples of both dsDNA and alpha-helical peptide bridges (multiple such bound alpha-helical bridges are shown in the example).

are the means and standard deviations for the set of pulses in Cluster 1 and 2 (Fig. S6C).

References:

1. O. Koniev, *et al.*, Selective irreversible chemical tagging of cysteine with 3-arylpropiolonitriles. *Bioconjug Chem* **25**, 202–206 (2014).

2. M. Petersheim, D. H. Turner, Base-stacking and base-pairing contributions to helix stability: thermodynamics of double-helix formation with CCGG, CCGGp, CCGGAp, ACCGGp, CCGGUp, and ACCGGUp. *Biochemistry* **22**, 256–263 (1983).

3. X. Zou, J. Wu, J. Gu, L. Shen, L. Mao, Application of Aptamers in Virus Detection and Antiviral Therapy. *Front. Microbiol.* **10** (2019).

4. Z. Chen, Q. Wu, J. Chen, X. Ni, J. Dai, A DNA Aptamer Based Method for Detection of SARS-CoV-2 Nucleocapsid Protein. *Virol. Sin.* **35**, 351–354 (2020).

5. Y. Song, *et al.*, Discovery of Aptamers Targeting the Receptor-Binding Domain of the SARS-CoV-2 Spike Glycoprotein. *Anal. Chem.* **92**, 9895–9900 (2020).

6. C. W. Fuller, *et al.*, Real-time single-molecule electronic DNA sequencing by synthesis using polymer-tagged nucleotides on a nanopore array. *Proc Natl Acad Sci U S A* **113**, 5233–5238 (2016).

7. S. Sorgenfrei, C. Chiu, M. Johnston, C. Nuckolls, K. L. Shepard, Debye Screening in Single-Molecule Carbon Nanotube Field-Effect Sensors. *Nano Lett.* **11**, 3739–3743 (2011).

8. P. B. Stranges, *et al.*, Design and characterization of a nanopore-coupled polymerase for single-molecule DNA sequencing by synthesis on an electrode array. *Proc Natl Acad Sci U S A* **113**, E6749–E6756 (2016).